Active Huygens' Box: Arbitrary Electromagnetic Wave Generation With an Electronically Controlled Metasurface

Alex M. H. Wong, *Senior Member, IEEE*, and George V. Eleftheriades, *Fellow, IEEE*

Abstract—This work investigates the generation of arbitrary electromagnetic waveforms inside a geometrical area enclosed by an active metasurface. We introduce the Huygens' box, where a region of space is enclosed by an active Huygens' metasurface. We show that, upon generating the necessary electric and magnetic currents, we can create any desired electromagnetic field inside Huygens' box. Using this method, we demonstrate, through simulation and experiment, the generation of traveling plane waves, a standing plane wave, and a Bessel wave inside a metallic cavity. These waves are generated using the same (reconfigurable) metasurface by aptly controlling the electronic excitations. By linear superposition of these unconventional traveling-wave "modes," we experimentally demonstrate, for the first time, a subwavelength superoscillation focal spot formed without involving evanescent EM waves and without an accompanying region of exorbitantly high waveform energy. The Huygens' box brings controlled waveform generation to an unprecedented level, with far-reaching implications to imaging, wireless communication, and medical therapy.

Index Terms—Active cloaking, cavity modes, equivalence principle, metasurface, super-resolution imaging, waveform synthesis.

I. INTRODUCTION

IN THE late 17th century, Christiaan Huygens proposed a theory on light propagation that later became a pillar of classical electromagnetics. His proposal, now known as Huygens' principle, stipulated that light propagates as a wave: the spatial locations reached by the wave would emanate secondary spherical wavelets that constructively interfere in the direction of light propagation [1]. While imperfect, Huygens' principle was a crucial part of the wave theory of light, which successfully explained light propagation phenomena, such as reflection, refraction, and diffraction off surfaces. Later refinements reconciled Huygens' principle with the mathematical formulation of electromagnetic waves. Fresnel [2] showed that upon adding an obliquity factor, Huygens' principle agrees with Kirchhoff's formulation of the scalar theory of electromagnetic waves. Love [3] and Schelkunoff [4] generalized Huygens' principle into the electromagnetic equivalence principle, which states that the electromagnetic fields within a region can be generated by equivalent sources in the form of surface currents (typically both electric and magnetic) at the region boundary. Today, the equivalence principle is regarded as a fundamental pillar of classical electromagnetics.

The recent development of electromagnetic metasurfaces [5]–[25]—artificially engineered surfaces possessing designer electromagnetic effects that are sometimes unfound in nature—can be understood in the perspective of Huygens' principle. Essentially, when illuminated by a known incident electromagnetic radiation, the subwavelength features on a metasurface produce the required secondary sources that interfere to generate the desired scattered field. Various demonstrations have showcased the metasurface as a ubiquitous tool that can perform anomalous reflection, refraction, and diffraction [6]–[10], lensing [11]–[13], subwavelength focusing [14]–[16], polarization manipulation [17]–[19], antenna beam shaping [20]–[22], holography, and image formation [23]–[25], among other applications. These works show that, by invoking Huygens' principle through an artificial planar structure, one can design an electromagnetic wave transformation device that is flexible, low profile, lightweight, and low cost compared with its replacement. By extension, one envisions that a greater degree of control can be achieved when a metasurface takes on a curved geometry in 3-D space [26]. More importantly, far greater flexibility can be endowed when the equivalent sources are active (impressed) instead of passively induced (secondary). Waveforms emanating from hard-to-realize original sources can now be conveniently synthesized by the metasurface; furthermore, these waveforms can be dynamically controlled by reconfiguring their electronic excitation. However, with few exceptions [27], [28], this area has, heretofore, remain unexplored.

This article demonstrates equivalence-inspired total wavefront control with a metasurface that wraps around a region of interest. We use an active Huygens' metasurface to excite the requisite electric and magnetic currents at the boundary of a square region that we call the Huygens' box, thus achieving unprecedented control of the fields inside the box. We show, through numerical simulation and experimental measurement, the synthesis of a standing wave, traveling waves, a Bessel
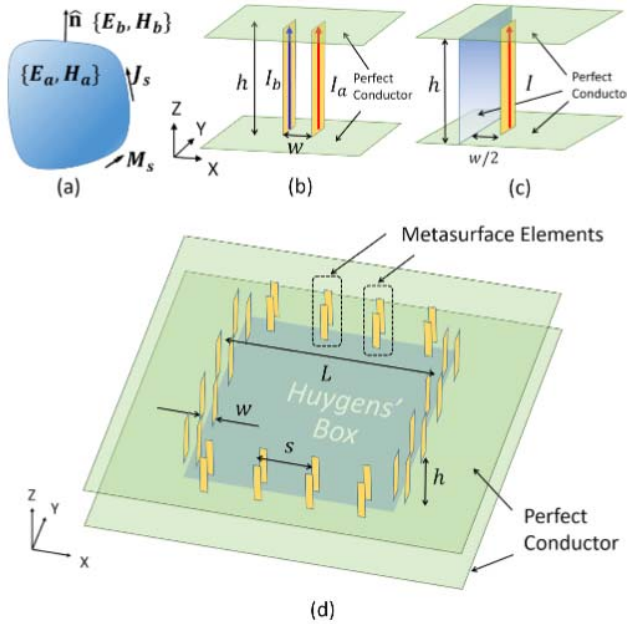
Fig. 1.   (Color) (a) Electromagnetic equivalence theory. A set of currents $\{J_s, M_s\}$ can generate an electromagnetic field $\{E_a, H_a\}$ within an enclosed area without affecting $\{E_b, H_b\}$ or adjust the electromagnetic field $\{E_b, H_b\}$ outside the area without affecting $\{E_a, H_a\}$. (b) Twin current filament that serves as the 2-D active Huygens' metasurface element. (c) Mirrored current filament that serves as a simplified 2-D active Huygens' metasurface element. (d) Schematic of Huygens' box, showing the 2-D environment and the placement of the twin current filaments.

wave, and a subwavelength focus inside Huygens' box. In particular, through the superposition of traveling waves, one can construct an arbitrary waveform within Huygens' box. This work demonstrates the direct usage of the electromagnetic equivalence principle to generate a class of waveforms, including waveforms whose existence is originally forbidden in their native environments (in this case, a metallic cavity). The Huygens' box allows one to generate and control an arbitrary electromagnetic waveform to unprecedented levels inside an enclosed area, with far-reaching ramifications in imaging, communication, and medical therapy.

II. THEORY

A. Electromagnetic Equivalence Principle

The equivalence principle is a fundamental principle in electromagnetics and states that multiple (equivalent) sources can produce the same electromagnetic field in a region of space [29]. One way of generating such an equivalent source is by exciting electric and magnetic currents at the boundary of a region of interest that generates the required electric and magnetic field discontinuities across it. When properly tuned, such an equivalent source boundary electromagnetically separates the regions inside and outside the boundary: each region is then able to assume an electromagnetic field distribution unaffected by the sources and field distribution in the other region.

We formalize the discussion by referring the reader to Fig. 1(a). Here, $\{E_a, H_a\}$ and $\{E_b, H_b\}$ represent the waves

inside and outside the boundary, respectively, $\hat{n}$ denotes the outward-pointing surface normal, and $\{J_s, M_s\}$ denote the electric and magnetic surface currents, which are given by

$$\begin{aligned} \mathbf{J_s} &= \hat{\mathbf{n}} \times (\mathbf{H_b} - \mathbf{H_a}) \\ \mathbf{M_s} &= -\hat{\mathbf{n}} \times (\mathbf{E_b} - \mathbf{E_a}). \end{aligned} \quad (1)$$

While the concept of electromagnetic equivalence is a theoretical topic for classical texts in electromagnetics [29], [30], recent advances in metasurfaces allow one to physically realize such currents and achieve, to an unprecedented level, the arbitrary generation and/or control of an electromagnetic waveform inside an enclosed environment. Especially, with a passive Huygens' metasurface [31]–[34], one can design the excited electric and magnetic currents along the surface that arise from a predefined incident wave and, thereby, achieves one-sided electromagnetic behavior. In this work, we demonstrate that by: 1) wrapping the metasurface to enclose a region and 2) using an active Huygens' metasurface, we can directly, actively, and arbitrarily tune the electromagnetic fields interior to the metasurface boundary without affecting the electromagnetic wave exterior to the metasurface boundary, and vice versa. This approach can achieve extreme transformations that are not possible with passive and/or planar Huygens' metasurfaces.

B. Huygens' Box Environment

To simplify the discussion of the conducted simulations and experiments, we consider a 2-D, TMz electromagnetic environment where all currents and fields remain invariant in the z-direction and the set of fields $\{H_x, H_y, E_z\}$ is nonzero in general. These conditions are met in a parallel-plate waveguide environment that we will discuss later in this article. In this environment, we define as our region of interest a square boundary of side length L enclosing the area $|x| \leq L/2$, $|y| \leq L/2$. We shall call this device the Huygens' box: in the following, we report arbitrary waveform generation inside this region through the proper excitation of electric and magnetic currents on its boundary.

C. Active Huygens' Metasurface

1) Twin Current Filament: We form a simple active Huygens' metasurface using the twin current filament as a Huygens' source element [35], [36]. As depicted in Fig. 1(b), this element consists of two line currents along the z-direction, equidistant from the metasurface boundary, which, for illustrative purposes, runs along the y-direction. The line source with current I_a is located just inside the Huygens' box, and the one with current I_b is located just outside. The currents I_a and I_b running through this source can be separated into an even (or copropgation) mode (I_e), which corresponds to an effective electric current in the z-direction, and an odd (or counter-propagation) mode (I_m), which corresponds to an effective magnetic current orthogonal to z and tangential to the metasurface direction. The even and odd mode currents

are obtained from the filament currents through

$$I_e = I_b + I_a$$
$$I_m = \frac{I_b - I_a}{2} \tag{2}$$

and the corresponding electric and magnetic surface currents are

$$\mathbf{J_s} = \frac{I_e}{s}\hat{\mathbf{z}}$$
$$\mathbf{M_s} = \frac{j\omega\mu_0 \ I_m w}{s}(\hat{\mathbf{n}} \times \hat{\mathbf{z}}). \tag{3}$$

Here, $\omega = 2\pi f$ is the angular frequency and μ_0 is the permeability of free space. As shown in Fig. 1(d), h, w, and s, respectively, denote the parallel-plate separation, line source separation, and unit cell size, and $\hat{\mathbf{n}}$ points outward (i.e., from current filament a to b). Upon rearranging (2) and (3), we arrive at

$$I_a = \frac{sJ_s}{2} + j\frac{sM_s}{\omega\mu_0 w}$$
$$I_b = \frac{sJ_s}{2} - j\frac{sM_s}{\omega\mu_0 w} \tag{4}$$

where s represents the separation between adjacent metasurface elements, $J_s = \mathbf{J_s} \cdot \hat{\mathbf{z}}$, $M_s = \mathbf{M_s} \cdot (\hat{\mathbf{n}} \times \hat{\mathbf{z}})$, and $\cdot$ denotes the inner product. Using (1) and (4), one can find the necessary surface currents, and then the corresponding excitation currents to the active Huygens' metasurface, that will synthesize or control the electromagnetic waveform in a desired manner.

2) Mirrored Current Filament: For situations where one wishes to synthesize an arbitrary waveform inside the enclosed region, but is unconcerned with electromagnetic waves outside the region, the twin current filament can be simplified into the mirrored current shown in Fig. 1(c). One arrives at the mirrored current filament by dissecting the twin current filament with a perfect conductor. Applying the electromagnetic image theory [29], one concludes that the perfect conductor serves as an antimirror to the single current filament. This effectively suppresses the electric surface current, doubles the magnetic surface current, and leaves unaffected the electromagnetic fields inside Huygens' box. Hence, somewhat counterintuitively, the remaining electric current filament I actually excites the odd mode, which synthesizes the magnetic surface current. Mathematically, in this arrangement, (4) simplifies to

$$I = j\frac{sM_s}{\omega\mu_0 w}. \tag{5}$$

Equations (1) and (5) can be used to calculate the currents required for waveform synthesis in Huygens' box excited with mirrored current filaments.

III. SIMULATIONS

A. Simulation Setup

Using the twin current filament configuration, we investigate the synthesis of electromagnetic waveforms inside the Huygens' box using the commercial full-wave electromagnetic simulator ANSYS High Frequency Structure Simulator (HFSS). Fig. 1(d) shows a diagram of the simulation. The simulation is performed at $f = 1$ GHz, with a corresponding free-space wavelength of $\lambda = 300$ mm. Two metallic conductors, spaced less than half-wavelength apart ($h = 44.5\text{mm} = 0.148\lambda$), form a parallel-plate environment that enforces the z-direction electromagnetic field invariance for all propagating modes. The simulation area is 2λ by 2λ in the xy plane and is terminated by a perfectly matched layer absorbing boundary. A Huygens' box with size $L = \lambda$ is generated at the center of the simulation domain, with element dimensions $s = \lambda/4$ and $w = \lambda/20$. In the following, we show simulation results using line sources, as depicted in Fig. 1(b), but, in practice, we find that the current filament can be replaced by a dipole or a monopole. We hypothesize that any small antenna with a matching current direction and a reasonably isotropic radiation pattern would serve the purpose since the field emanating from such an antenna would couple similarly into the propagating modes of the parallel-plate environment.

B. Synthesizing Arbitrary Traveling Waves

We first demonstrate the generation of traveling plane waves within the Huygens' box. The electric and magnetic fields for a plane wave propagating at an angle θ with respect to the x-axis can be written as follows:

$$\mathbf{E}(x, y) = E_0 e^{-j(k_x x + k_y y)} \hat{\mathbf{z}}$$
$$\mathbf{H}(x, y) = \frac{E_0}{\eta_0} e^{-j(k_x x + k_y y)}(\sin\theta \ \hat{\mathbf{x}} - \cos\theta \ \hat{\mathbf{y}}) \tag{6}$$

where $\eta = \sqrt{\mu_0/\varepsilon_0}$ is the characteristic impedance of free space, $k_x = k_0 \cos\theta$, $k_y = k_0 \sin\theta$, and $k_0 = 2\pi/\lambda$. In this article, we assume an $e^{j\omega t}$ time dependence. To synthesize such a traveling plane wave in the Huygens' box, we find $\{\mathbf{E_a}(x, y), \mathbf{H_a}(x, y)\}$ by solving (6) at the metasurface boundary, and setting $\{\mathbf{E_b}, \mathbf{H_b}\}$ to zero, we can write (1) as

$$\mathbf{J_s}(x, y) = -\hat{\mathbf{n}} \times \mathbf{H_a}(x, y)$$
$$\mathbf{M_s}(x, y) = \hat{\mathbf{n}} \times \mathbf{E_a}(x, y). \tag{7}$$

Solving (7) yields the surface currents $\{\mathbf{J_s}(x, y), \mathbf{M_s}(x, y)\}$ along the metasurface boundary. To implement this surface current, the surface is discretized into a finite set of locations, each of which will be synthesized with a pair of current filaments, as shown in Fig. 1(b) and (d). In general, an element spacing of less than half-wavelength is sufficient to generate the desired waveform. We will elaborate on this topic in Section VI. Upon determining the unit cell locations, the results of (7) can be substituted into (4) to calculate a set of filament currents $\{I_a, I_b\}$, which forms our excitation to the active Huygens' metasurface. Thereafter, we observe the generation of the field profile $\{\mathbf{E_a}(x, y), \mathbf{H_a}(x, y)\}$ upon applying the excitation currents $\{I_a, I_b\}$ in the simulation. Fig. 2 shows, at four time instants, the time-varying electric field in the simulation environment, corresponding to the generation of three plane waves, with propagation angles of $\theta_1 = 0°$, $\theta_2 = 30°$, and $\theta_3 = 45°$ with respect to the x-axis (horizontal). From these plots, it is clear that a traveling wave is produced
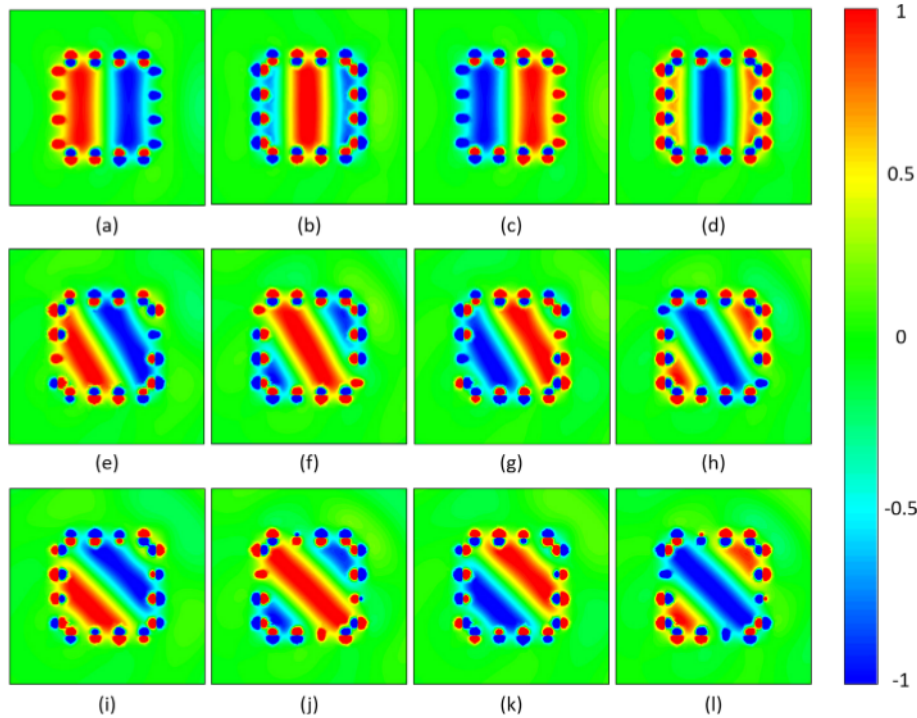
Fig. 2. (Color) Full-wave simulation results for generating plane waves inside the Huygens' box. Generation of three plane waves, propagating at (a)–(d) $\theta_1 = 0°$, (e)–(h) $\theta_2 = 30°$, and (i)–(l) $\theta_3 = 45°$ from the x-axis (horizontal). For each angle of propagation, the instantaneous electric field $E_z(x, y, t)$ is plotted at four different phase points, each spaced 90° apart.

inside the parallel-plate environment at the prescribed angles; it is also clear that the traveling wave is generated only inside the confines of Huygens' box, even without the presence of a hard boundary (such as a perfect conductor) at the edge of the box to preclude the penetration of the electromagnetic wave. As expected, regions of large field amplitudes exist in the vicinity of the line sources, but the field level decays quickly away from these elements, such that at about an eighth of a wavelength away from the current locations, the traveling plane wave profiles can be clearly observed. By enabling the generation of arbitrary plane waves in an enclosed region, any electromagnetic wave can be synthesized as a superposition of plane waves.

C. Mimicking and Cloaking Electromagnetic Fields

The functionality of the Huygens' box is not limited to cases where external fields are absent. Fig. 3(a) shows a case where a traveling wave at $\theta_i = 60°$ is twisted 90° clockwise within the confines of the box. In this case, the metasurface excitation $\{I_a, I_b\}$ synthesizes within the Huygens' box the superposition of two plane waves: 1) a traveling wave at $\theta_i = 60°$ with the same amplitude but opposite phase to that of the incident wave and 2) another traveling wave at $\theta_{HB} = 150°$. The first wave cancels the incident electromagnetic field, while the second generates the field profile, as shown in Fig. 3(a). Fig. 3(b)–(d) shows that, in this situation [see Fig. 3(b)], an object inside the Huygens' box would assume a scattering pattern that differs from the scattering pattern upon illumination at $\theta_i = 60°$

[see Fig. 3(c)] and approximates the scattering pattern upon illumination at $\theta_{i,eff} = 150°$ [see Fig. 3(d)]. Small imperfections lead to slight spurious scattering that causes ripples in Fig. 3(a), as well as slight deviations between Fig. 3(b) and (d). We expect that these deviations would diminish for a larger Huygens' box. Since the waveform inside the Huygens' box can be synthesized at will, the Huygens' box facilitates endless possibilities for mimicking or engineering the scattering profile of any contained object.

Fig. 3(e)–(h) shows the special case where the total field vanishes inside the Huygens' box. Because of this absence of electromagnetic fields, the objects inside the box do not scatter and are effectively cloaked from the external illumination. Fig. 3(f)–(h) shows the absence of scattering when a metal box [see Fig. 3(f)], a cluster of metallic cylinders [see Fig. 3(g)], and a cluster of ceramic cylinders [see Fig. 3(h)] are, respectively, placed inside the Huygens' box. We emphasize that the same set of currents is used in all four situations. This shows that while the currents depend on the cloaking boundary and the external field, they do not change with the size, shape, or material of the cloaked object. The cloaking and mimicking properties of an active source boundary were proposed in [37]–[39], as theoretical works involving scalar (for example, acoustic) waves. In the electromagnetic domain, similar functionalities were investigated under the study of transformation optics [40], [41] and, more recently, active electromagnetic cloaking [28], [42]. The Huygens' box that we hereby propose, represents an advancement over previous explorations in which: 1) we have shown that many
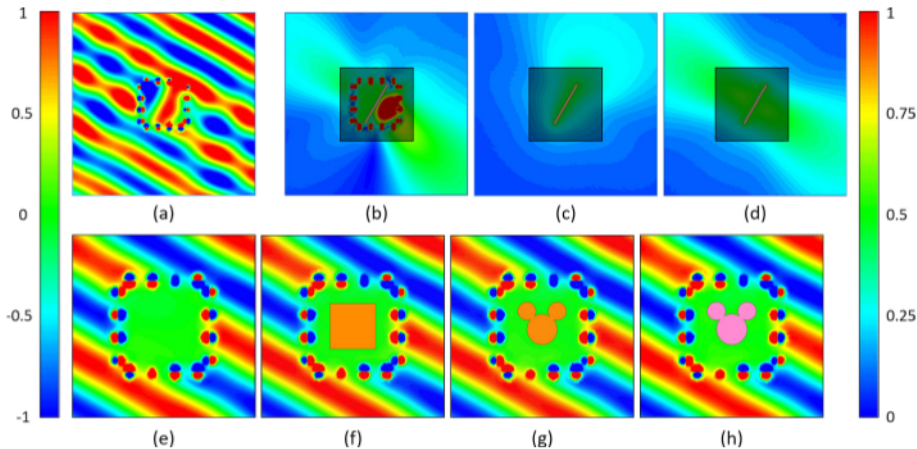
Fig. 3. (Color) Mimicking and cloaking with the Huygens' box. (a) Electric field distribution when the Huygens' box is excited to turn an incident plane wave at $\theta_i = 60°$ into one propagating at $\theta_{HS} = 150°$ inside the box. (b) Scattering from a metallic plate placed inside the Huygens' box of (a). (c) Scattering from the same metallic plate without the Huygens' box ($\theta_i = 60°$). (d) Scattering from the same metallic plate when the incident wave impinges at $\theta_i = 150°$. (e) Electric field distribution when the Huygens' box is excited to generate a zero-field region upon plane wave incidence at $\theta_i = 60°$. (f)–(h) Electric field distribution of the Huygens' box in (e) when (f) a metallic box, (g) a collection of metallic cylinders, and (h) a collection of ceramic cylinders (Al$_2$O$_3$, $\varepsilon_r = 9.8$) are placed inside the Huygens' box. The instantaneous electric field is plotted for (a) and (e)–(h) (the color bar on the left applies); the electric field phasor amplitude is plotted for (b)–(d) (the color bar on the right applies). For (b)–(d), the region inside, and immediately outside, the Huygens' box is shaded in gray to emphasize the scattering pattern, which is best seen at some distance away from the Huygens' box.

of the tantalizing possibilities achievable with transformation optics are also achievable with a Huygens' box arrangement with dramatic improvements in simplicity and compactness compared with the former and 2) we have shown, in full-wave simulation analysis, that arbitrary waveform generation, cloaking, and scattering engineering are possible with vectorial electromagnetic waves.

IV. EXPERIMENT

A. Experimental Apparatus

We proceed to experimentally demonstrate the generation of arbitrary waveforms within a Huygens' box. To simplify the experiment, we adopt the mirrored current filament as our Huygens' metasurface element. A schematic of the experimental apparatus is shown in Fig. 4(a). The experiment is facilitated by a two-port Agilent programmable network analyzer (PNA). For the purpose of this experiment, we use ports 1 and 2 as the transmit and receive ports, respectively. A signal at the test frequency is sent from port 1 of the PNA and then evenly split into 16 portions by a 1-to-16 power divider. The 16 channels are fed into an RF circuit board shown in Fig. 4(b). On this circuit board, computer-controlled bias signals regulate the attenuators and phase-shifters to attenuate the amplitude and shift the phase of each RF signal as desired. Hence, complete amplitude and phase tuning is afforded to individually control all 16 RF channels. After amplitude and phase adjustment, the 16 RF signals drive 16 monopole antennas located within the Huygens' box, which is shown in Fig. 4(c) and (d). As previously explained, monopole antennas function similar to current filaments with respect to their coupling to propagating modes within the parallel-plate environment. They are chosen in this implementation of Huygens' box because of their easy installation. Since the mirrored current filament metasurface element features a

metallic backing, this effectively turns the Huygens' box into a metallic cavity, with monopole antenna excitations spaced at subwavelength separations. The key device dimensions are $L = 300$ mm, $s = 75$ mm, $w_{sep} = w/2 = 20$ mm, and $h = 44.5$ mm. An aluminum plate with hexagonal perforations serves as the top cover of Huygens' box. The perforations are deeply subwavelength to forbid the leakage of electromagnetic waves but allow the penetration of a coaxial cable probe that measures the electric field within the Huygens' box. A mechanical scanner scans the measurement probe across the xy plane located at the vertical center of the Huygens' box. The probe electrically connects to port 2 of the PNA, such that the resultant S_{21} reading on the PNA correlates linearly to a measurement of the z-directed electric field phasor (E_z) within the Huygens' box.

B. Plane-Wave Excitation

We first demonstrate the synthesis of a plane wave within the cavity. Fig. 5(a) and (c) shows, at one moment in time, the experimentally measured E_z over the cavity for two traveling plane waves, with $\theta_1 = 0°$ and $\theta_2 = 45°$ with respect to the x-axis. Fig. 5(b) and (d) shows the corresponding simulation results. As one can observe, good agreement is obtained between experiment and simulation, and both demonstrate the generation of a traveling wave inside our Huygens' box. The superposition of such traveling waves leads to the generation of other interesting waveforms. For example, Fig. 5(e) and (f) shows the experimental and simulated generation of a standing wave pattern formed by the equiamplitude superposition of two traveling waves in the $+x$- and $-x$-directions. It is of interest to note that the demonstrated waveforms feature very strong electric field components tangential to and in subwavelength proximity to the metallic cavity walls. While such waves would not exist in a conventional metallic cavity,
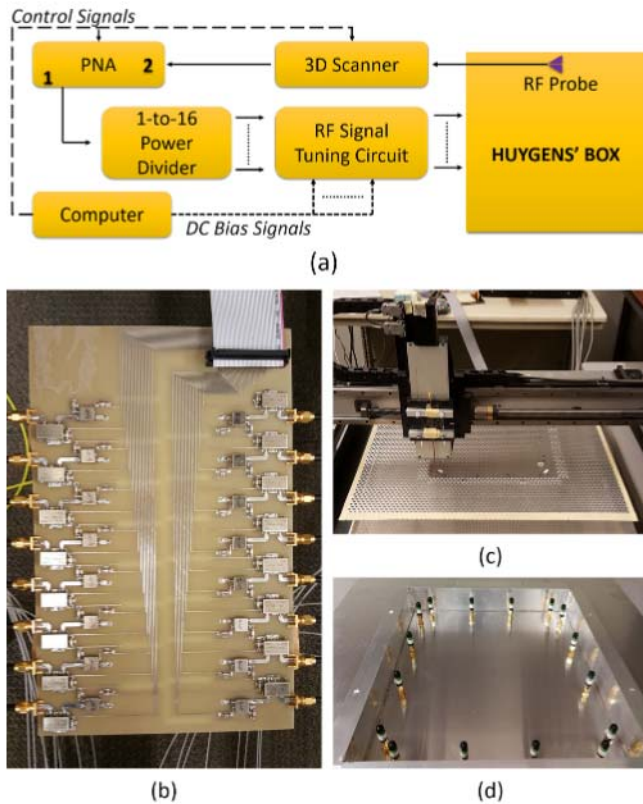
Fig. 4. (Color) Experimental demonstration of the Huygens' box. (a) Signal flow diagram for the Huygens' box experiment. Solid, dashed, and dotted lines, respectively, denote RF signals, control signals, and dc biases. (b) The 16-channel RF tuning circuit. (c) The 3-D scanner and the Huygens' box. (d) The Huygens' box with the top plate removed, showing the box geometry and the monopole antenna elements.

they can be excited as unconventional "modes" when the corresponding excitation is applied to the active metasurface. Furthermore, their combination allows one to form a wide range of waveforms within this Huygens' box.

C. Bessel-Wave Excitation

We proceed to synthesize a Bessel function focus within this Huygens' box. The electromagnetic profile for the Bessel focal waveform is [29]

$$\mathbf{E}(r) = E_0 \, J_0(k_0 \, r) \, \hat{\mathbf{z}}$$
$$\mathbf{H}(r) = j\frac{E_0}{\eta_0} J_1(k_0 r) \, \hat{\boldsymbol{\phi}} \qquad (8)$$

where $J_n(\cdot)$ represents the nth-order Bessel function of the first kind, $r = \sqrt{x^2 + y^2}$, and $\hat{\boldsymbol{\phi}} = -\sin\theta \, \hat{\mathbf{x}} + \cos\theta \, \hat{\mathbf{y}}$. One may calculate the necessary Huygens' box excitation by directly substituting (8) into (1) and (5). Alternatively, one may invoke the Fourier–Bessel transform to express the Bessel waveform as an integral over a continuum of plane waves that travel in every direction orthogonal to z and constructively interfere at the origin

$$|\mathbf{E}(r)| = E_0 \, J_0(k_0 \, r) = E_0 \int_0^{2\pi} e^{-jk_0(x\cos\theta + y\sin\theta)} \, d\theta \, . \qquad (9)$$

We adopt the latter method and then find the excitation currents as a superposition of the excitation currents needed to generate the constituent plane waves.

Fig. 5(g) and (h) demonstrates the measured and simulated electric field profile of a Bessel waveform. Again, simulation and experiment agree to show the successful generation of the Bessel waveform inside the Huygens' box. The Bessel waveform is typically generated as modes in a circular waveguide; furthermore, only a discrete set of Bessel waveforms, whose electric field nulls appear at the waveguide walls, can be generated for a circular waveguide of a specific size. However, with our method, a Bessel waveform with an arbitrary spatial frequency k_0 can be synthesized within a rectangular cavity, as long as the corresponding frequency lies within the operation bandwidth of the Huygens' box. Once again, this exemplifies the versatility of the Huygens' box as a device for the generation of arbitrary electromagnetic waveforms.

V. Subwavelength Focusing in the Huygens' Box

Finally, we demonstrate the generation of a subwavelength-focused superoscillation electromagnetic waveform in the Huygens' box. Due to the unique scientific contribution associated with this waveform, we have grouped into this section the background, simulation, and experimental aspects of this work.

A. Background and Motivation

Since the pioneering works of Abbé [44] and Rayleigh [45] on the resolution of imaging systems, it has long been understood that the resolution of an electromagnetic wave is limited to about half its wavelength. In recent decades, we witnessed the emergence of electromagnetic imaging systems with much higher resolution, which makes use of evanescent electromagnetic waves, chemical fluorescent labels, and other forms of prior information [46]–[52]. However, these methods are plagued by some combination of drawbacks, such as the requirement of prior sample preparation, fine-step scanning with step sizes of $\lambda/10$ or less, short working distances of $\lambda/10$ or less, intensive data postprocessing, and restriction to a very specific class of imaged objects.

More recently, it has been shown that propagating waves can achieve super-resolution using a wave phenomenon called superoscillation [53]–[56]. By interfering slow-varying waves, regions of sharp variations can be obtained wherein the waveform oscillates faster than the fastest constituent waveform. Through this phenomenon, propagating plane waves of relatively slow spatial variation can interfere to form fast variations of multiple oscillations per wavelength, or hotspots of a smaller size than predicted by the Abbé diffraction limit, over a selected region. In this manner, super-resolution can be obtained inside a selected region without the involvement of evanescent waves, hence alleviating drawbacks involved with highly reactive energy components. Using EM waves that are superoscillatory in the spatial and/or temporal domains, researchers have demonstrated the formation of subwavelength hotspots as well as far-field super-resolution microscopes [16], [57]–[64]. However, a major drawback to
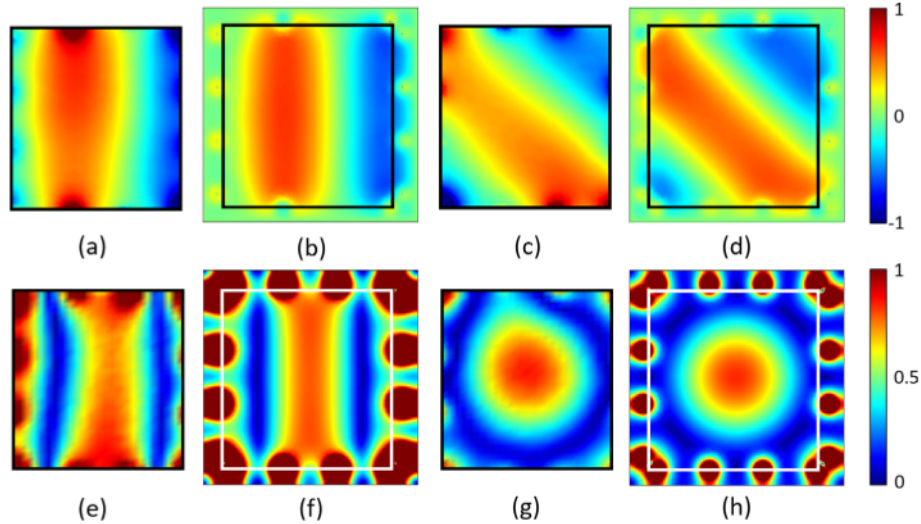
Fig. 5.   (Color) Experimental and full-wave simulation results of electromagnetic wave synthesis with the Huygens' box. The black rectangles indicate the coverage extent of the measurement probe in the experiment. (a) Measured and (b) simulated synthesis of a plane wave propagating with $\theta_1 = 0°$. (c) Measured and (d) simulated synthesis of a plane wave propagating with $\theta_1 = 45°$. (e) Measured and (f) simulated synthesis of a standing wave. (g) Measured and (h) simulated synthesis of the zeroth-order Bessel function focus. The instantaneous electric field is plotted for (a)–(d). The electric field phasor amplitude is plotted for (e)–(h).

such superoscillation waveforms is the existence of a non-superoscillatory high-energy region [65]. The existence of this high-energy region is proven to be mathematically inevitable; furthermore, the waveform energy is proven to scale aggressively with the rate and duration of the superoscillation feature. Examples of superoscillation waveforms, constructable with propagating waves, are shown in Fig. 6(a) and (b). In both cases, subwavelength features are generated at the expense of high wave amplitudes outside the superoscillation region. The high-energy region poses a stringent limit to the rate and duration of the superoscillation. Moreover, its existence highly increases the energy and/or sensitivity cost of the super-resolution system and can lead to spurious scattering by particles that fall in the high-energy region. While methods have been proposed to sidestep disadvantages associated with the high-energy region, its existence remains a hurdle for the widespread deployment of superoscillation-based imaging systems [66]. This work presents, to the best of our knowledge, the first experimental demonstration on synthesizing a subwavelength focal spot using superoscillations, without generating the accompanying high-energy region.

B. Selective Superoscillation Generation

Although the existence of the high-energy region is shown to be unavoidable in a mathematical analysis of waves with infinite support (for example, a wave in free space) [65], the presence of a metasurface boundary introduces new possibilities for waveform synthesis. In a previous work [67], we have theoretically shown that one can strategically place a closed metasurface boundary such that it encloses the super-resolution region of a superoscillation waveform but excludes the high-energy region. In this manner, the super-oscillatory hotspot is synthesized devoid of the high-energy

region, hence eliminating the possibility of spurious scattering from the high-energy region and dramatically reducing the energy cost of generating such superoscillation hotspots [67]. Fig. 6(b) shows the electric field profile for a superposition of plane waves that form a 1-D subwavelength focus at a prescribed focal plane $x = 0$. This superoscillation waveform is designed as a combination of plane waves

$$\mathbf{E}(x, y) = \sum_{n=0}^{N-1} E_n e^{-jk_{nx}x} \cos(k_{ny}y) \, \hat{\mathbf{z}}$$

$$\mathbf{H}(x, y) = \sum_{n=0}^{N-1} \frac{E_n}{\eta_0} e^{-jk_{nx}x} \left(-j\frac{k_{ny}}{k_0} \sin(k_{ny}y) \, \hat{\mathbf{x}} \right.$$
$$\left. - \frac{k_{nx}}{k_0} \cos(k_{ny}y) \, \hat{\mathbf{y}} \right) \quad (10)$$

where

$$k_{nx} = -k_0 + \left(n + \frac{1}{2}\right)\left(\frac{2k_0}{N}\right)$$

$$k_{ny} = \sqrt{k_0^2 - k_{nx}^2} \quad (11)$$

and $\{E_n\}$ is a set of complex coefficients chosen through a zero-placement method adapted from antenna array design [43], [58]. Table I tabulates the values for $\{E_n\}$.

The electric field profile along the image plane is displayed in Fig. 6(e) (red dotted line) and compared with the diffraction limit (black dashed–dotted line). As one can observe from Fig. 6(e), this waveform is squeezed beyond the diffraction limit at the focal plane. If this waveform is generated in free space, one must tolerate the accompanying high-energy regions along the y-axis. Beyond this, it is also typical to find higher energy regions at some longitudinal distance (in the x-direction) away from the focal plane. To avoid these high-energy regions, we strategically place a Huygens' box
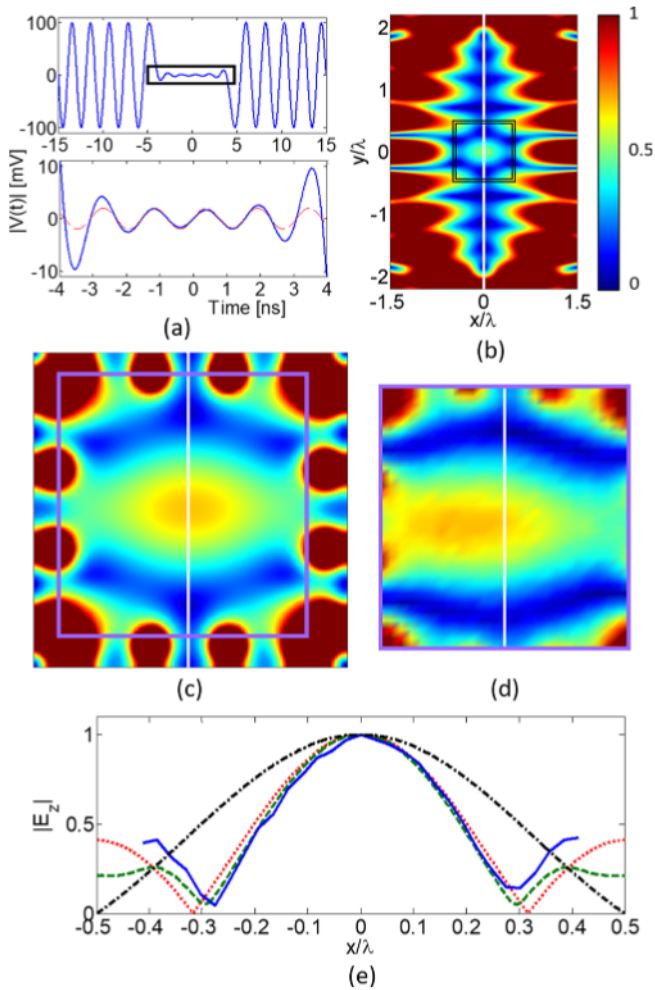
Fig. 6. (Color) Superoscillation function generation using a Huygens' box. (a) Example of a time-domain superoscillation waveform with a bandwidth of 500 MHz (blue solid line). The boxed section in the top panel is shown in a close-up in the bottom figure and found comparable to a sinusoid oscillating at 650 MHz (red dashed lines) (adopted from [43]). (b) Superposition of plane waves leading to a superoscillatory subwavelength focus along the imaging plane (white solid line). The electric field distribution is plotted in a region surrounding the image plane. The proposed Huygens' box location is also depicted (black double-box). (c) Simulated electric field distribution within the Huygens' box. (d) Measured electric field distribution within the Huygens' box. (e) Electric field distribution at the focal plane. The compared waveforms are obtained from theory (red dotted line), simulation (green dashed line) and measurement (blue solid line), and the theoretical 1-D diffraction-limited sinc (black dashed–dotted line).

TABLE I
ELECTRIC FIELD WEIGHTS FOR A SUBDIFFRACTION
SUPEROSCILLATION WAVEFORM

n	E_n [n.u.]	n	E_n [n.u.]	n	E_n [n.u.]
0	1.0000	21	0.0352	42	0.0183
1	-0.4961	22	0.0465	43	-0.0017
2	-0.3302	23	0.0510	44	-0.0218
3	-0.1917	24	0.0481	45	-0.0389
4	-0.0768	25	0.0388	46	-0.0496
5	0.0108	26	0.0247	47	-0.0515
6	0.0689	27	0.0080	48	-0.0433
7	0.0989	28	-0.0086	49	-0.0251
8	0.1042	29	-0.0227	50	0.0016
9	0.0908	30	-0.0320	51	0.0331
10	0.0648	31	-0.0353	52	0.0648
11	0.0331	32	-0.0320	53	0.0908
12	0.0016	33	-0.0227	54	0.1042
13	-0.0251	34	-0.0086	55	0.0989
14	-0.0433	35	0.0080	56	0.0689
15	-0.0515	36	0.0247	57	0.0108
16	-0.0496	37	0.0388	58	-0.0768
17	-0.0389	38	0.0481	59	-0.1917
18	-0.0218	39	0.0510	60	-0.3302
19	-0.0017	40	0.0465	61	-0.4961
20	0.0183	41	0.0352	62	1.0000

from earlier works on superoscillation, we have constructed a subwavelengh hotspot without the generation of a high-energy region. Fig. 6(e) shows the plots of the waveform distribution along the focal plane and shows good agreement among the theoretical (red dotted line), simulated (green dashed–dotted line), and measured (blue solid line) electric field profiles. All these profiles achieve subwavelength focusing: the spot widths are clearly reduced from the sinc waveform that characterizes the 1-D Abbé diffraction limit (black dashed–dotted line). Stronger subwavelength focusing is achievable with a more aggressive design of the current weights.

VI. DISCUSSION

In Sections II–V, we have presented theory, simulation, and experimental measurements, showing the ability to produce arbitrary EM waves within an enclosed region using the concept of the Huygens' box. Here, we discuss a few features of interest and present results that can form the basis of further investigations.

A. Relation to the Total-Field/Scattered-Field Scheme

The numerical implementation of generating electromagnetic fields inside a boundary of field or current sources has been known in computational electromagnetics as the total-/scatter-field method [68]. Using this method, arbitrary soft sources are implemented in the "total-field" computation region only. This helps avoid expansive simulations involving far-field sources and alleviates unwanted effects, such as the source field's interaction with the boundary of the computation

[as outlined in Fig. 6(b)] to include the region with the subwavelength hotspot but exclude the region of high-energy sidelobes. As before, we find the current excitations required to synthesize this subwavelength hotspot by substituting (10) into (1) and (4). Fig. 6(c) shows the simulated selective generation of this superoscillation waveform in the Huygens' box. As demonstrated here, one can include only the superoscillation region in the Huygens' box and, thereby, exclude the high-energy regions. Fig. 6(d) and (e) shows the experimental measurement that confirms the simulation result and demonstrates the generation of a waveform that is focused beyond the diffraction limit. Again, in a departure
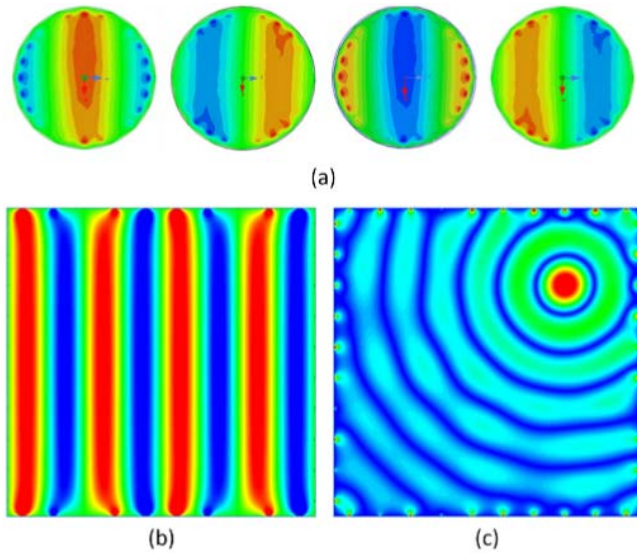
Fig. 7. (Color) Waveform generation in Huygens' boxes of different shapes and sizes. (a) Traveling wave with $\theta = 0$ within a cylindrical Huygens' box. (E_z plotted at four time instants.) (b) Traveling wave with $\theta = 0$ (E_z plotted at an instant in time). (c) Bessel wave centered at $x = \lambda$, $y = \lambda$ (phasor amplitude of E_z plotted). In (b) and (c), both waves are generated in a $4\lambda \times 4\lambda$ Huygens' box, with ten elements on each side spaced 0.4λ apart.
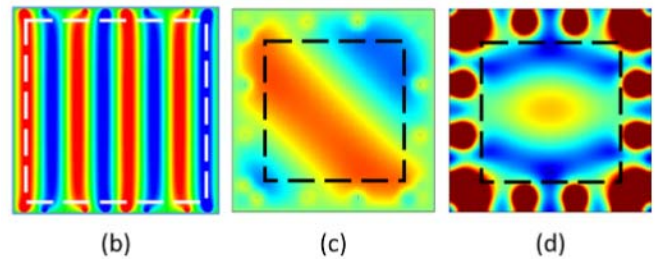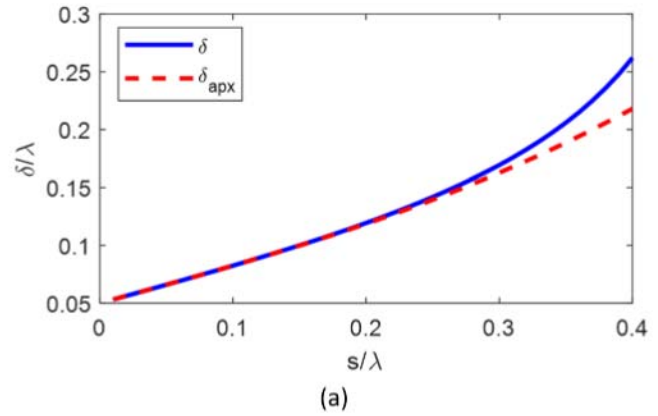

Fig. 8. (Color) Effects of element spacing on the synthesized waveform. (a) Plot showing the discrepancy region as a function of element spacing. A metasurface thickness $w_{sep} = 0.05\lambda$ is assumed. (b)–(d) Few waveforms generated by Huygens' box (simulation results) with the extent of the discrepancy region denoted by the dashed lines. (The discrepancy region is exterior to the dashed line.)

domain. While both the electromagnetic equivalence theory and the total-field/scattered-field method find applications in theoretical and computational electromagnetics, the current work proposes a physical implementation through the concept of the Huygens' box. Similar to the TF/SF formulation, the Huygens' box can be used to synthesize an arbitrary incident waveform in a compact space, without spurious interactions between the source and the scattered waveform, the measurement apparatus, or structures outside the total-field region. In addition, we also expect the Huygens' box to share similar properties to the TF/SF formulation in aspects such as relation to external fields and implementation possibilities for an enclosed region of arbitrary size and shape. We shall elaborate on these aspects in Sections VI-B and C.

B. Interaction With External Fields

Having situated the current work with respect to the TF/SF formulation in Section VI-A, we proceed to comment on the Huygens' box's interaction with external fields also in this context. In essence, the open Huygens' box (as discussed in Sections II and III) generates an electromagnetic field $\{E_a - E_b, H_a - H_b\}$ independent of external fields [see Fig. 1(a)]. This EM field superimposes with fields $\{E_b, H_b\}$ already inside the box due to the presence of external sources. The overall result is the generation of a total field $\{E_a, H_a\}$ inside the Huygens' box.

In actual implementation, external fields may couple into Huygens' metasurface sources and, thereby, perturb the fields generated by the Huygens' box. Care must be taken in feed network design, such that excitation to Huygens' sources by external fields is properly treated. In the current work, the sources are made nonresonant such that there is weak coupling among the sources and between the source and any

external field. Furthermore, the feed network is impedance matched to minimize spurious reradiations, which may alter the field generated inside the Huygens' box. An interesting future direction involves using Huygens' sources as both receivers and transmitters. A receive circuit deciphers information of the external field as received from the sources. After processing by electronic circuitry and/or computer calculation, the transmit circuit drives the same source elements to generate the corresponding electric and magnetic currents, which will generate the desired field $\{E_a, H_a\}$ according to (1). This achievement may, for example, render adaptive the active cloak displayed in Fig. 3(e)–(h) and lead to a host of powerful applications limited only by designer imagination.

C. 3-D Huygens' Box of Arbitrary Size and Shape

While in this work, we present investigations of the Huygens' box in a 2-D square formation, we envision further development toward a 3-D closed surface of arbitrary size and shape. To begin with, one can straightforwardly construct a Huygens' box of an arbitrary 2-D profile. For example, Fig. 7(a) shows the simulated traveling wave in a cylindrical Huygens' box [69]. To synthesize a Huygens' box in 3-D space, one needs a metasurface that can generate electric and magnetic currents in arbitrary directions. The currents can be synthesized by various sources: while in this work, we build our active Huygens' metasurface element from ground-backed monopoles, various Huygens' sources and magnetodielectric antennas [34], [70] would also serve
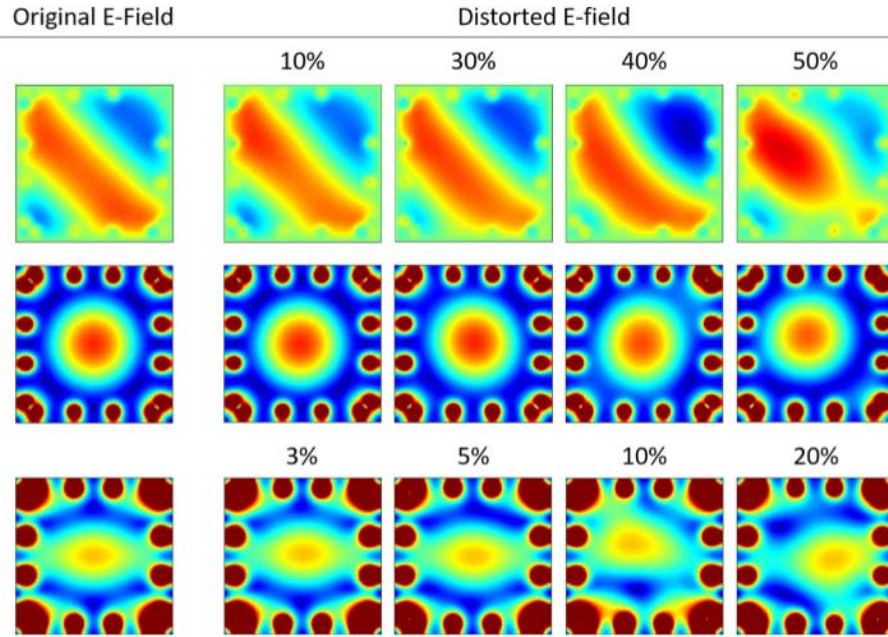
Fig. 9. (Color) Sensitivity analysis. The generated waveforms upon introducing a random-phased additive white Gaussian error signal with various mean strengths for the error signal. $\mathbf{E}_z$ at a time instant is plotted for the plane wave (first row), while the electric field phasor amplitude is plotted for the Bessel function focus and the superoscillatory hotspot (second and third rows).

well as active Huygens' metasurface elements. As we will discuss in Section VI-D, as long as these metasurface elements are spaced less than half-wavelength apart, the metasurface satisfies the Nyquist–Shannon sampling theorem [71] and, hence, can faithfully synthesize all propagating waveforms. The viability of the 3-D Huygens' box has been amply demonstrated in many numerical simulations involving the TF/SF method. Notwithstanding, to arrive at a physical implementation, one needs to resolve various practical issues, such as efficiently exciting a large number of sources with the required amplitude, phase, and current directions, avoiding or compensating for mutual coupling effects, and so on. A practical 3-D Huygens' box of arbitrary shape may open doors to numerous applications, including imaging, sensing, and extreme RCS design.

D. Effects of Element Spacing

We now investigate the effect of element spacing on the waveform generated inside the Huygens' box. In simple terms, the Nyquist–Shannon sampling theorem states that a sampling frequency of double the spectrum of a signal suffices to represent the signal accurately [71]. Applied to the space and spatial frequency domains, a discrete source of element spacing s suffices to synthesize an electromagnetic waveform with a transverse spatial frequency spectrum $k_t \in [-k_{t,max}, k_{t,max}]$, where

$$k_{t,max} = \pi/s . \tag{12}$$

As the Huygens' box generates an arbitrary waveform through the superposition of propagating waves, the waveform has a transverse wavevector spectrum $k_t \in [-k_0, k_0]$. Through (12),

we see that a waveform covering this spectrum can be accurately generated by the Huygens' box with an element spacing $s = \lambda/2$. However, near the Huygens' box boundary, the near-field of the discrete electric and magnetic current sources will cause deviations from the desired waveform. A finer element spacing shall reduce this region of discrepancy by extending the synthesized spatial frequency spectrum to also include a part of the evanescent wave spectrum.

While the exact extent of this region of discrepancy depends on the desired waveform and the near-field of a Huygens' source element, in the following, we present a reasonable estimate on how far this discrepancy region should extend from the boundary of the Huygens' box. We first represent with t and p the transverse and longitudinal directions of the metasurface in consideration; the $p > 0$ region represents the interior of the Huygens' box. Suppose that, with the element spacing s_0, where $s_0 < \lambda/2$, along the metasurface, we achieve accurate spatial spectrum representation across the range $[-k_{t0}, k_{t0}]$. The most gradual decay component of the discrepancy will come from an evanescent plane wave with a transverse spatial frequency k_{t0}^+. Through the constitutive relationship, we find the corresponding longitudinal spatial frequency as $k_p = \sqrt{k_0^2 - k_{t0}^2}$. k_p is purely imaginary as $k_{t0} > k_0$. Thus, the attenuation constant is $\alpha_p = |\Im\{k_p\}|$. The evanescent wave can, thus, be written as

$$\mathbf{E}_{\mathbf{evnst}}(t, p) = \mathbf{E_0}e^{-jk_{t0}t}e^{-\alpha_p p} . \tag{13}$$

This wave will attenuate in the $+p$-direction and will decay to e^{-1} of the original field amplitude at a distance $1/\alpha_p$ from the Huygens' box boundary. Other components of the discrepancy will feature $k_t > k_{t0}$ and, therefore, decay more

rapidly. Accounting for our use of a metasurface element with a nonzero thickness of w_{sep}, we, hence, estimate with

$$\delta = w_{sep} + \frac{1}{\alpha_p} \qquad (14)$$

the region from the Huygens' box boundary within which we may expect appreciable discrepancy due to the discreteness of Huygens' sources. Applying simple algebra with the above-mentioned relations, we find that

$$\delta = w_{sep} + \frac{s}{\pi\sqrt{1-(2s/\lambda)^2}}$$
$$\delta_{apx} = w_{sep} + \frac{s}{\pi}\left(1 + 2\left(\frac{s}{\lambda}\right)^2\right). \qquad (15)$$

Here, δ_{apx} is the first-order Taylor's series approximation of δ for $(2s/\lambda)^2 \ll 1$.

Fig. 8(a) shows the plots of δ and δ_{apx} as a function of element spacing for $0.01\lambda < s < 0.4\lambda$, for a typical value of $w_{sep} = 0.05\lambda$. We observe that, for a relatively large separation of $s = 0.4\lambda$, $\delta \simeq w_{sep} + s/2$, but, for smaller separations ($s < 0.2\lambda$), $\delta \simeq w_{sep} + s/\pi$. The approximation δ_{apx} closely matches δ, especially for small values of s: it approaches within 4% of δ for $s < 0.3\lambda$. Fig. 8(b)–(d) overlays the respective discrepancy regions atop the simulated wave generated in Figs. 5(d), 6(c), and 7(b). For Fig. 8(b), the Huygens' box size, element spacing, and estimated discrepancy region are 4λ, $s = 0.4\lambda$, and $\delta = 0.22\lambda$, respectively. For Fig. 8(c) and (d), respective figures are box size: 1λ, elemental spacing: $s = 0.25\lambda$, and discrepancy region: $\delta = 0.16\lambda$. It can be observed that all three waveforms are faithfully generated beyond the discrepancy region.

While the true extent of such a discrepancy region depends on the actual waveform and the Huygens' sources used, the discrepancy distance δ that we derive here serves well as a conservative limit: it tends to overestimate the discrepancy region since it considers the evanescent wave component that decays the most gradually. In most situations, a substantial amount of the near-field lies in evanescent components with more rapid decay, which tends to reduce the discrepancy region.

E. Sensitivity Analysis

We now investigate, through simulation, the sensitivity of the generated waveforms with respect to the current weights. We do this by adding a random-phased white Gaussian error signal to each complex current weight in the 16-element Huygens' box. Fig. 9 shows the plots of the synthesized waveform in the presence of typical error signals. The mean powers of the error signal, as labeled on the figure, are referenced as a percentage of the highest of the 16 excitation currents. Fig. 9 represents the typical waveform distortion due to imprecise current excitation. As can be observed, the plane wave (first row) retains its shape upon the addition of an error signal whose mean current is 30%–40% of the signal current. The Bessel wavefront, formed by constructive interference of plane waves, is more robust: the focal spot undergoes only
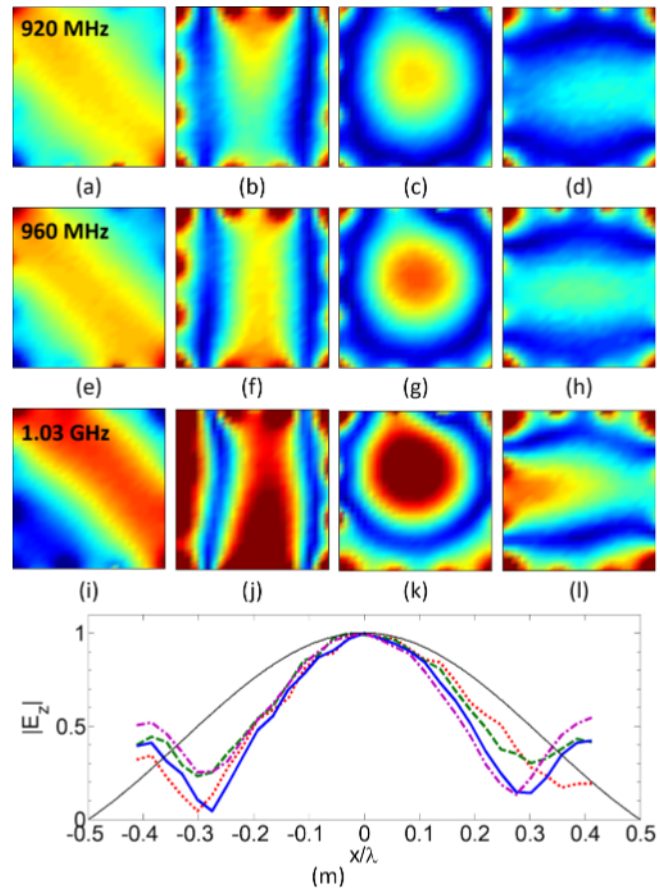

Fig. 10. (Color) Bandwidth estimation for the Huygens' box. (a)–(d) Experimentally measured waveform at (a)–(d) 920 MHz, (e)–(h) 960 MHz, and (i)–(l) 1.03 GHz. The waveforms generated are a traveling wave with $\theta = 45°$ (a), (e) and (i), a standing wave in the x-direction (horizontal) (b), (f), and (j), (c) Bessel waveform (c), (g), and (k), and (a) superoscillation subwavelength focus (d), (h), and (l). (m) Focal width of the superoscillation waveform as a function of frequency. The shown frequencies are 920 MHz (red dotted line), 960 MHz (green dotted line), 1 GHz (blue solid line), 1.03 GHz (purple dashed–dotted line), and the 1-GHz diffraction limited sinc function (black thin line).

minor changes at an error strength of up to 40% and shifts by a small distance of 0.08λ when the error signal's mean strength reaches 50%. On the other hand, the subwavelength superoscillatory focal spot, which attains its subwavelength size through an intricate destructive interference of the constituent plane waves, is less tolerant to error. Notwithstanding, the hotspot and its surrounding silent region remain intact with the addition of a 5% mean error. Beyond this level, the hotspot and its surrounding silent region start to shift in location, but the hotspot remains visible at a mean error as large as 20%. The analysis suggests that the waveforms generated are reasonably robust to imprecise current excitations, which bodes well for the practical generation of a wide range of waveforms.

F. Bandwidth Analysis

We also briefly discuss the typical bandwidth for the Huygens' box. The bandwidth for an arbitrary waveform synthesis device depends on many factors, including the nature of the

waveform one wishes to generate, the spectral response of the source, the tuning circuit, and the metasurface element. In this work, while we design the metasurface current weights to synthesize waveforms at an operational frequency of 1 GHz, we find that waveform synthesis is achieved over a reasonable bandwidth of about 11% surrounding this frequency, both for the traveling plane waves and the subwavelength-focused superoscillatory wave. Fig. 10 shows the experimentally measured electric field profile for the generation of four waveforms—the 45° traveling plane wave, the standing wave, the Bessel wave, and the superoscillatory subwavelength focus—at frequencies of 0.92 [see Fig. 10(a)–(d)], 0.96 [see Fig. 10(e)–(h)], and 1.03 GHz [see Fig. 10(i)–(l)], respectively. Despite slight deviations, the traveling plane wave is reasonably synthesized. For the superoscillatory subwavelength focus, Fig. 10(m) shows the focal field pattern at the image plane as a function of frequency. As shown, for a bandwidth of 11% around 1 GHz, subwavelength focusing is achieved with the selective excitation of propagating waves. While the bandwidths quoted here are achieved without spectral considerations at the design stage, the operational bandwidth of the Huygens' box can be dramatically extended when one takes care to employ broadband components and frequency-tuned excitations [70]. In this latter case, one can further tune a broadband version of the Huygens' box to achieve frequency-dependent waveforms, hence unlocking an extra dimension of waveform control of great importance to many applications [72].

VII. CONCLUSION

In this article, we examined the synthesis of arbitrary electromagnetic waveforms inside a region enclosed by an active Huygens' metasurface. We introduced an effective 2-D environment that we name the Huygens' box, within which we have demonstrated, by calculation, simulation, and experimental measurement, the generation of arbitrary electromagnetic waveforms through proper excitation of the enclosing active Huygens' metasurface. We have shown the ability of the Huygens' box to perform cloaking and electromagnetic-field mimicking operations. We have also demonstrated the generation of traveling, standing, and Bessel waveforms inside a Huygens' box enclosed within a metallic cavity even though these waveforms cannot exist within a conventional metallic cavity. Finally, we used a Huygens' box to generate a subwavelength focus of propagating waves without exciting the corresponding high-energy region, thus achieving a wave profile very useful for super-resolution electromagnetic focusing and imaging. We emphasize that all waveforms are synthesized by applying suitable dc electronic biases to configure the metasurface excitation. The presented Huygens' box, hereby, takes electromagnetic waveform control and synthesis to an unprecedented level. We expect it to find promising applications in controlling electric and/or magnetic field profiles in various cloaking, medical imaging, and antenna applications that feature the use of electromagnetic waves in open, enclosed, or partially enclosed geometries.

REFERENCES

[1] C. Huygens, *Traité de la Lumiere*, P. van der Aa, Ed. London, U.K.: Mamillan, 1912.

[2] A. Fresnel, "Mémoire sur la diffraction de la lumière," *Paris, Impr. Imperial*, vol. 1, pp. 247–363, 1870.

[3] A. E. H. Love, "The integration of the equations of propagation of electric waves," *Philos. Trans. Roy. Soc. London A, Contain. Papers Math. Phys. Character*, vol. 197, pp. 1–45, Jan. 1901.

[4] S. A. Schelkunoff, "Some equivalence theorems of electromagnetics and their application to radiation problems," *Bell Syst. Tech. J.*, vol. 15, no. 1, pp. 92–112, Jan. 1936.

[5] C. L. Holloway, M. A. Mohamed, E. F. Kuester, and A. Dienstfrey, "Reflection and transmission properties of a metafilm: With an application to a controllable surface composed of resonant particles," *IEEE Trans. Electromagn. Compat.*, vol. 47, no. 4, pp. 853–865, Nov. 2005.

[6] N. Yu *et al.*, "Light propagation with phase discontinuities: Generalized laws of reflection and refraction," *Science*, vol. 334, no. 6054, pp. 333–337, Oct. 2011.

[7] M. Kim, A. M. H. Wong, and G. V. Eleftheriades, "Optical Huygens' metasurfaces with independent control of the magnitude and phase of the local reflection coefficients," *Phys. Rev. X*, vol. 4, no. 4, Dec. 2014, Art. no. 041042. [Online]. Available: http://link.aps.org/doi/10.1103/PhysRevX.4.041042

[8] N. Mohammadi Estakhri and A. Alù, "Wave-front transformation with gradient metasurfaces," *Phys. Rev. X*, vol. 6, no. 4, Oct. 2016, Art. no. 041008.

[9] A. Díaz-Rubio, V. S. Asadchy, A. Elsakka, and S. A. Tretyakov, "From the generalized reflection law to the realization of perfect anomalous reflectors," *Sci. Adv.*, vol. 3, no. 8, Aug. 2017, Art. no. e1602714.

[10] A. M. H. Wong and G. V. Eleftheriades, "Perfect anomalous reflection with a bipartite Huygens' metasurface," *Phys. Rev. X*, vol. 8, no. 1, Feb. 2018, Art. no. 011036.

[11] F. Aieta *et al.*, "Aberration-free ultrathin flat lenses and axicons at telecom wavelengths based on plasmonic metasurfaces," *Nano Lett.*, vol. 12, no. 9, pp. 4932–4936, Aug. 2012.

[12] X. Ni, S. Ishii, A. V. Kildishev, and V. M. Shalaev, "Ultra-thin, planar, babinet-inverted plasmonic metalenses," *Light Sci. Appl.*, vol. 2, no. 4, p. e72, Apr. 2013.

[13] K. Chen *et al.*, "A reconfigurable active Huygen's metalens," *Adv. Mater.*, vol. 29, no. 17, p. 1606422, Feb. 2017.

[14] A. Grbic, L. Jiang, and R. Merlin, "Near-field plates: Subdiffraction focusing with patterned surfaces," *Science*, vol. 320, no. 5875, pp. 511–513, Apr. 2008.

[15] L. Markley, A. M. H. Wong, Y. Wang, and G. V. Eleftheriades, "Spatially shifted beam approach to subwavelength focusing," *Phys. Rev. Lett.*, vol. 101, no. 11, Sep. 2008, Art. no. 113901.

[16] E. T. F. Rogers *et al.*, "A super-oscillatory lens optical microscope for subwavelength imaging," *Nature Mater.*, vol. 11, no. 5, pp. 432–435, May 2012.

[17] Z. Bomzon, G. Biener, V. Kleiner, and E. Hasman, "Space-variant Pancharatnam–Berry phase optical elements with computer-generated subwavelength gratings," *Opt. Lett.*, vol. 27, no. 13, pp. 1141–1143, Jul. 2002.

[18] C. Pfeiffer and A. Grbic, "Cascaded metasurfaces for complete phase and polarization control," *Appl. Phys. Lett.*, vol. 102, no. 23, Jun. 2013, Art. no. 231116.

[19] M. Selvanayagam and G. V. Eleftheriades, "Polarization control using tensor Huygens surfaces," *IEEE Trans. Antennas Propag.*, vol. 62, no. 12, pp. 6155–6168, Dec. 2014.

[20] R. Leberer and W. Menzel, "A dual planar reflectarray with synthesized phase and amplitude distribution," *IEEE Trans. Antennas Propag.*, vol. 53, no. 11, pp. 3534–3539, Nov. 2005.

[21] J. Hunt *et al.*, "Metamaterial apertures for computational imaging," *Science*, vol. 339, no. 6117, pp. 310–313, Jan. 2013.

[22] A. Epstein, J. P. S. Wong, and G. V. Eleftheriades, "Cavity-excited Huygens' metasurface antennas for near-unity aperture illumination efficiency from arbitrarily large apertures," *Nature Commun.*, vol. 7, no. 1, p. 10360, Jan. 2016.

[23] B. Walther *et al.*, "Spatial and spectral light shaping with metamaterials," *Adv. Mater.*, vol. 24, no. 47, pp. 6300–6304, Oct. 2012.

[24] X. Ni, A. V. Kildishev, and V. M. Shalaev, "Metasurface holograms for visible light," *Nature Commun.*, vol. 4, no. 2807, Nov. 2013.

[25] D. Wen *et al.*, "Helicity multiplexed broadband metasurface holograms," *Nature Commun.*, vol. 6, no. 1, p. 8241, Sep. 2015.

[26] A. Diaz-Rubio, J. Li, C. Shen, S. Cummer, and S. Tretyakov, "Power-flow conformal metamirrors for engineering wave reflections," 2017, *arXiv:1710.06336*. [Online]. Available: http://arxiv.org/abs/1710.06336

[27] P.-Y. Chen and A. Alú, "Mantle cloaking using thin patterned metasurfaces," *Phys. Rev. B, Condens. Matter*, vol. 84, no. 20, Nov. 2011, Art. no. 205110.

[28] M. Selvanayagam and G. V. Eleftheriades, "An active electromagnetic cloak using the equivalence principle," *IEEE Antennas Wireless Propag. Lett.*, vol. 11, pp. 1226–1229, Oct. 2012.

[29] R. F. Harrington, *Time-Harmonic Electromagnetic Fields* (IEEE Pass Series on Electromagnetic Wave Theory). Piscataway, NJ, USA: IEEE Press, 2001.

[30] C. A. Balanis, *Advanced Engineering Electromagnetics*. Hoboken, NJ, USA: Wiley, 1989.

[31] C. Pfeiffer and A. Grbic, "Metamaterial Huygens' surfaces: Tailoring wave fronts with reflectionless sheets," *Phys. Rev. Lett.*, vol. 110, no. 19, May 2013, Art. no. 197401.

[32] M. Selvanayagam and G. V. Eleftheriades, "Discontinuous electromagnetic fields using orthogonal electric and magnetic currents for wavefront manipulation," *Opt. Express*, vol. 21, no. 12, pp. 14409–14429, Jun. 2013.

[33] A. Epstein and G. V. Eleftheriades, "Huygens' metasurfaces via the equivalence principle: Design and applications," *J. Opt. Soc. Amer. B, Opt. Phys.*, vol. 33, no. 2, pp. A31–A50, Feb. 2016.

[34] M. Chen, M. Kim, A. M. H. Wong, and G. V. Eleftheriades, "Huygens' metasurfaces from microwaves to optics: A review," *Nanophotonics*, vol. 7, no. 6, pp. 1207–1231, Jun. 2018.

[35] A. M. H. Wong and G. V. Eleftheriades, "A simple active Huygens source for studying waveform synthesis with Huygens metasurfaces and antenna arrays," in *Proc. IEEE Int. Symp. Antennas Propag.*, Jul. 2015, pp. 1092–1093.

[36] A. M. H. Wong and G. V. Eleftheriades, "Active Huygens' metasurfaces for RF waveform synthesis in a cavity," in *Proc. IEEE Medit. Electrotechnical Conf. (MELECON)*, Apr. 2016, pp. 1–5.

[37] D. A. B. Miller, "On perfect cloaking," *Opt. Express*, vol. 14, no. 25, pp. 12457–12466, Dec. 2006.

[38] F. G. Vasquez, G. W. Milton, and D. Onofrei, "Active exterior cloaking for the 2D laplace and Helmoltz equations," *Phys. Rev. Lett.*, vol. 103, no. 7, Aug. 2009, Art. no. 073901.

[39] H. H. Zheng, J. J. Xiao, Y. Lai, and C. T. Chan, "Exterior optical cloaking and illusions by using active sources: A boundary element perspective," *Phys. Rev. B, Condens. Matter*, vol. 81, no. 19, May 2010, Art. no. 195116.

[40] J. B. Pendry, "Controlling electromagnetic fields," *Science*, vol. 312, no. 5781, pp. 1780–1782, Jun. 2006.

[41] Y. Lai *et al.*, "Illusion optics: The optical transformation of an object into another object," *Phys. Rev. Lett.*, vol. 102, no. 25, Jun. 2009, Art. no. 253902.

[42] M. Selvanayagam and G. V. Eleftheriades, "Experimental demonstration of active electromagnetic cloaking," *Phys. Rev. X*, vol. 3, no. 4, Nov. 2013, Art. no. 041011.

[43] A. M. H. Wong and G. V. Eleftheriades, "Temporal pulse compression beyond the Fourier transform limit," *IEEE Trans. Microw. Theory Techn.*, vol. 59, no. 9, pp. 2173–2179, Sep. 2011.

[44] E. Abbé, "Beiträge zur Theorie des Mikroskops und der mikroskopischen Wahrnehmung," *Archiv für Mikroskopische Anatomie*, vol. 9, no. 1, pp. 413–468, 1873.

[45] L. Rayleigh, "On pin-hole photography," *London, Edinburgh, Dublin Philos. Mag. J. Sci.*, vol. 31, no. 189, pp. 87–99, 1891.

[46] E. H. Synge, "A suggested method for extending microscopic resolution into the ultra-microscopic region," *Philos. Mag.*, vol. 6, no. 35, pp. 356–362, Aug. 1928.

[47] E. A. Ash and G. Nicholls, "Super-resolution aperture scanning microscope," *Nature*, vol. 237, no. 5357, pp. 510–512, Jun. 1972.

[48] D. W. Pohl, W. Denk, and M. Lanz, "Optical stethoscopy: Image recording with resolution $\lambda/20$," *Appl. Phys. Lett.*, vol. 44, no. 7, pp. 651–653, Apr. 1984.

[49] J. B. Pendry, "Negative refraction makes a perfect lens," *Phys. Rev. Lett.*, vol. 85, no. 18, pp. 3966–3969, Oct. 2000.

[50] S. W. Hell and J. Wichmann, "Breaking the diffraction resolution limit by stimulated emission: Stimulated-emission-depletion fluorescence microscopy," *Opt. Lett.*, vol. 19, no. 11, pp. 780–782, 1994.

[51] M. J. Rust, M. Bates, and X. Zhuang, "Sub-diffraction-limit imaging by stochastic optical reconstruction microscopy (STORM)," *Nat. Methods*, vol. 3, no. 10, pp. 793–795, 2006.

[52] A. Szameit *et al.*, "Sparsity-based single-shot subwavelength coherent diffractive imaging," *Nature Mater.*, vol. 11, no. 5, pp. 455–459, May 2012.

[53] Y. Aharonov, J. Anandan, S. Popescu, and L. Vaidman, "Superpositions of time evolutions of a quantum system and a quantum time-translation machine," *Phys. Rev. Lett.*, vol. 64, no. 25, pp. 2965–2968, Jun. 1990.

[54] M. V. Berry, *Faster than Fourier* (Quantum Coherence and Reality: In Celebration of the 60th Birthday of Yakir Aharonov). Singapore: World Scientific, 1994, pp. 55–65.

[55] A. M. H. Wong and G. V. Eleftheriades, "Advances in imaging beyond the diffraction limit," *IEEE Photon. J.*, vol. 4, no. 2, pp. 586–589, Apr. 2012.

[56] M. Berry *et al.*, "Roadmap on superoscillations," *J. Opt.*, vol. 21, no. 5, Apr. 2019, Art. no. 053002.

[57] F. M. Huang, Y. Chen, F. J. G. de Abajo, and N. I. Zheludev, "Optical super-resolution through super-oscillations," *J. Opt. A, Pure Appl. Opt.*, vol. 9, no. 9, pp. S285–S288, Aug. 2007.

[58] A. M. H. Wong and G. V. Eleftheriades, "Adaptation of Schelkunof's superdirective antenna theory for the realization of superoscillatory antenna arrays," *IEEE Antennas Wireless Propag. Lett.*, vol. 9, pp. 315–318, Apr. 2010.

[59] A. M. H. Wong and G. V. Eleftheriades, "Sub-wavelength focusing at the multi-wavelength range using superoscillations: An experimental demonstration," *IEEE Trans. Antennas Propag.*, vol. 59, no. 12, pp. 4766–4776, Dec. 2011.

[60] S. Kosmeier, M. Mazilu, J. Baumgartl, and K. Dholakia, "Enhanced two-point resolution using optical eigenmode optimized pupil functions," *J. Opt.*, vol. 13, no. 10, Sep. 2011, Art. no. 105707.

[61] A. M. H. Wong and G. V. Eleftheriades, "Superoscillatory radar imaging: Improving radar range resolution beyond fundamental bandwidth limitations," *IEEE Microw. Wireless Compon. Lett.*, vol. 22, no. 3, pp. 147–149, Mar. 2012.

[62] A. M. H. Wong and G. V. Eleftheriades, "An optical super-microscope for far-field, real-time imaging beyond the diffraction limit," *Sci. Rep.*, vol. 3, no. 1, p. 1715, Dec. 2013.

[63] D. Tang *et al.*, "Ultrabroadband superoscillatory lens composed by plasmonic metasurfaces for subdiffraction light focusing," *Laser Photon. Rev.*, vol. 9, no. 6, pp. 713–719, Nov. 2015.

[64] X. H. Dong, A. M. H. Wong, M. Kim, and G. V. Eleftheriades, "Superresolution far-field imaging of complex objects using reduced superoscillating ripples," *Optica*, vol. 4, no. 9, pp. 1126–1133, Sep. 2017.

[65] P. J. S. G. Ferreira and A. Kempf, "Superoscillations: Faster than the nyquist rate," *IEEE Trans. Signal Process.*, vol. 54, no. 10, pp. 3732–3740, Oct. 2006.

[66] N. I. Zheludev, "What diffraction limit?" *Nature Mater.*, vol. 7, no. 6, pp. 420–422, Jun. 2008.

[67] A. M. H. Wong and G. V. Eleftheriades, "Superoscillations without sidebands: Power efficient sub-diffraction imaging with propagating waves," *Sci. Rep.*, vol. 5, no. 8449, Feb. 2015.

[68] A. Taflove and S. C. Hagness, *Computational Electrodynamics: The Finite-Difference Time-Domain Method*, 3rd ed. Norwood, MA, USA: Artech House, 2005.

[69] K. A. Oyesina, O. Z. Aly, G. G. L. Zhou, and A. M. H. Wong, "Active Huygens' box: Arbitrary synthesis of em waves in metallic cavities," in *Proc. Int. Appl. Comput. Electromagn. (ACES) Symp.*, Apr. 2019, pp. 1–2.

[70] K.-M. Luk and B. Wu, "The magnetoelectric dipole—A wideband antenna for base stations in mobile communications," *Proc. IEEE*, vol. 100, no. 7, pp. 2297–2307, Jul. 2012.

[71] C. E. Shannon, "Communication in the presence of noise," *Proc. IRE*, vol. 37, no. 1, pp. 10–21, 1949.

[72] A. M. H. Wong and G. V. Eleftheriades, "Broadband superoscillation brings a wave into perfect three-dimensional focus," *Phys. Rev. B, Condens. Matter*, vol. 95, no. 7, Feb. 2017, Art. no. 075148.
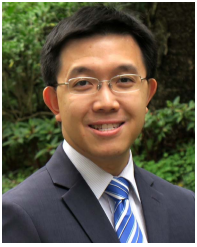
Alex M. H. Wong (Senior Member, IEEE) received the B.A.Sc. degree in engineering science (electrical option) and the M.A.Sc. and Ph.D. degrees in electrical and computer engineering from the University of Toronto, Toronto, ON, Canada, in 2006, 2009, and 2014, respectively.

He then briefly served as a Post-Doctoral Fellow at the University of Toronto. Since 2018, he has been an Assistant Professor of applied electromagnetics with the Department of Electronic Engineering, City University of Hong Kong (CityU), Hong Kong,
where he is also a member of the State Key Laboratory of Terahertz and Millimeter Waves. He has advanced multiple projects in applied electromagnetics on next-generation RF, infrared and optical metasurfaces, and super-resolution imaging and radar systems. Particularly, he has made academic contributions to research on wave shaping using Huygens' metasurfaces and far-field imaging based on superoscillation waves. His current research interests include metasurfaces, metamaterials, and super-resolution systems.

Dr. Wong is a member of the IEEE Antennas and Propagation Society, Microwave Theory and Techniques Society and the Photonics Society. He serves as the TPC Vice-Chair for the 2020 Asia–Pacific Microwave Conference. He has taken on various programme committees as the Session Chair and Technical Judge and reviewer duties for the IEEE conferences and journal publications in the AP and MTT societies, as well as relevant venues in applied physics. His received accolades include the IEEE RWP King Award (for the best annual publication by a young author in the IEEE TRANSACTIONS ON ANTENNAS AND PROPAGATION), the URSI Young Scientist Award, the Raj Mittra Grant, the IEEE Doctoral Research Awards from the AP and MTT Societies, and the Canada Graduate Scholarship (doctoral level).

George V. Eleftheriades (Fellow, IEEE) received the Diploma degree in electrical engineering from the National Technical University of Athens, Athens, Greece, and the M.S.E.E. and Ph.D. degrees in electrical engineering from the University of Michigan, Ann Arbor, MI, USA, in 1989 and 1993, respectively.

From 1994 to 1997, he was with the Swiss Federal Institute of Technology, Lausanne, Switzerland. Currently, he is a Professor with the Department of Electrical and Computer Engineering, University of
Toronto, Toronto, ON, Canada, where he holds the Velma M. Rogers Graham Chair in Nano- and Micro-Structured Electromagnetic Materials. He is a recognized international authority and pioneer in the area of metamaterials. These are man-made materials, which have electromagnetic properties not found in nature. He introduced a method for synthesizing metamaterials using loaded transmission lines. Together with his graduate students, he provided the first experimental evidence of imaging beyond the diffraction limit and pioneered several novel antennas and microwave components using these transmission-line-based metamaterials. His research has impacted the field by demonstrating the unique electromagnetic properties of metamaterials, used in lenses, antennas, and other microwave and optical components to drive innovation in fields, such as wireless and satellite communications, defence, medical imaging, microscopy, and automotive radar. Presently, he is leading a group of graduate students and researchers in the areas of electromagnetic and optical metamaterials, metasurfaces, antennas and components for broadband wireless communications, novel antenna beam-steering techniques, far-field super-resolution imaging, radars, plasmonic and nanoscale optical components, and fundamental electromagnetic theory.

Dr. Eleftheriades also served as a member of the IEEE AP-Society Administrative Committee (AdCom) from 2007 to 2012 and was an IEEE AP-S Distinguished Lecturer from 2004 to 2009. In 2009, he was elected as a fellow of the Royal Society of Canada. Papers that he coauthored have received numerous awards, such as the 2009 Best Paper Award from the IEEE MICROWAVE AND WIRELESS PROPAGATION LETTERS, twice the R. W. P. King Best Paper Award from the IEEE TRANSACTIONS ON ANTENNAS AND PROPAGATION in 2008 and 2012, and the 2014 Piergiorgio Uslenghi Best Paper Award from the IEEE ANTENNAS AND WIRELESS PROPAGATION LETTERS. He received the Ontario Premier's Research Excellence Award and the University of Toronto's Gordon Slemon Award, both in 2001. In 2004, he received the E.W.R. Steacie Fellowship from the Natural Sciences and Engineering Research Council of Canada. In 2018, he received the Research Leader Award from the Faculty of Applied Science and Engineering of the University of Toronto. He was a recipient of the 2008 IEEE Kiyo Tomiyasu Technical Field Award, the 2015 IEEE John Kraus Antenna Award, and the 2019 IEEE Antennas and Propagation Distinguished Achievement Award. He served as the General Chair for the 2010 IEEE International Symposium on Antennas and Propagation held in Toronto. He served as an Associate Editor for the IEEE TRANSACTIONS ON ANTENNAS AND PROPAGATION (AP).